

REPORT DOCUMENTATION PAGE

AFRL-SR-AR-TR-06-0377

Public reporting burden for this collection of information is estimated to average 1 hour per response, including the time for gathering and maintaining the data needed, and completing and reviewing the collection of information. Send comments regarding this burden estimate or any aspect of this collection of information, including suggestions for reducing this burden, to Washington Headquarters Services, Directorate for Information Operations and Reports, 1215 Jefferson Davis Highway, Suite 1204, Arlington, VA 22202-4302, and to the Office of Management and Budget, Paperwork Reduction Project (0704-0188).

1. AGENCY USE ONLY (Leave blank)		2. REPORT DATE	3. REPORT TYPE AND DATES COVERED 01 Jan 2003 - 31 Dec 2005 FINAL	
4. TITLE AND SUBTITLE INSTABILITIES, SEPARATION AND TRANSITION IN THREE-DIMENSIONAL BOUNDARY LAYERS, WITH EMPHASIS ON GAS-TURBINE-BLADE FLOWS			5. FUNDING NUMBERS 61102F 2304/BX	
6. AUTHOR(S) DR RYZHOV				
7. PERFORMING ORGANIZATION NAME(S) AND ADDRESS(ES) UNIVERSITY OF CALIFORNIA SPONSORED PROGRAMS DAVIS CA 95616-5270			8. PERFORMING ORGANIZATION REPORT NUMBER	
9. SPONSORING/MONITORING AGENCY NAME(S) AND ADDRESS(ES) AFOSR/NE 4015 WILSON BLVD SUITE 713 ARLINGTON VA 22203 <i>Dr Arge Nachman</i>			10. SPONSORING/MONITORING AGENCY REPORT NUMBER  F49620-03-1-0043	
11. SUPPLEMENTARY NOTES				
12a. DISTRIBUTION AVAILABILITY STATEMENT DISTRIBUTION STATEMENT A: Unlimited			12b. DISTRIBUTION CODE	
13. ABSTRACT (Maximum 200 words) 1. Gortler vortices on the concave pressure side of a blade 2. Laminar/turbulent transition on the convex side of a blade 3. Turbulent separation under the action of the strong adverse pressure gradient 4. Cooling-film aerodynamics				
14. SUBJECT TERMS			15. NUMBER OF PAGES	
			16. PRICE CODE	
17. SECURITY CLASSIFICATION OF REPORT Unclassified		18. SECURITY CLASSIFICATION OF THIS PAGE Unclassified	19. SECURITY CLASSIFICATION OF ABSTRACT Unclassified	20. LIMITATION OF ABSTRACT UL

# **Final report on research on instabilities, separation and transition in three-dimensional boundary layers with emphasis on gas-turbine-blade flows**

Grant F49620-03-1-0043

*Oleg S. Ryzhov*

Department of Mechanical and Aeronautical Engineering  
University of California, Davis

## **Introduction**

Due to very large curvature of both sides of a typical turbine blade, the flow past each of them has specific features not intrinsic to wing aerodynamics. The Figure below illustrates this statement, showing a long region of laminar/turbulent transition on the upper (suction) side and absolutely unstable Görtler vortices adjacent to the lower (pressure) side. The streamwise pressure gradient is favourable over most of the suction side and adverse on the pressure side that provokes turbulent separation. Thus, the types of instabilities to be expected to develop on each side should be different in nature. Turbulent separation under the influence of the strong adverse pressure gradient is an additional poorly understood phenomenon characteristic of turbomachinery flows. Up to recently, all these topics were beyond the scope of any rigorous mathematical treatment, challenging theoreticians to develop a pertinent high-Reynolds number asymptotic approach which would cover, along with instabilities, also late (or deep) transition. Traditionally, transition is regarded as the most intricate stage of flow on the turbine/compressor blade even as compared to fully developed turbulence. However, turbulent velocity fields are hardly amenable to analytical study. Only a few attempts were made to attack the simplest case of the zero-pressure-gradient flow on a flat plate without introducing special assumptions on the closure model. Previous theoretical studies of turbulent separation involved crude errors. Thus, the proposed research is aimed at resolving long-standing difficult problems of fundamental importance from both scientific and industrial standpoints, especially as applied to gas-turbine engine aerodynamics.

More specifically, the work done under the grant started on January 1, 2003 encompasses the following topics:

1. Görtler vortices on the concave pressure side of a blade;
2. Laminar/turbulent transition on the convex side of a blade;
3. Turbulent separation under the action of the strong adverse pressure gradient;
4. Cooling-film aerodynamics.

In fact, the cooling-film flows fall beyond the scope of the proposal, but a shift in priorities in transition on gas-turbine blades made it timely to extend the contents of the proposed research so as to cover this new important issue. Note that to simplify notation, a separate numbering of equations and figures, as well as a separate list of references, is used in each of the sections below.

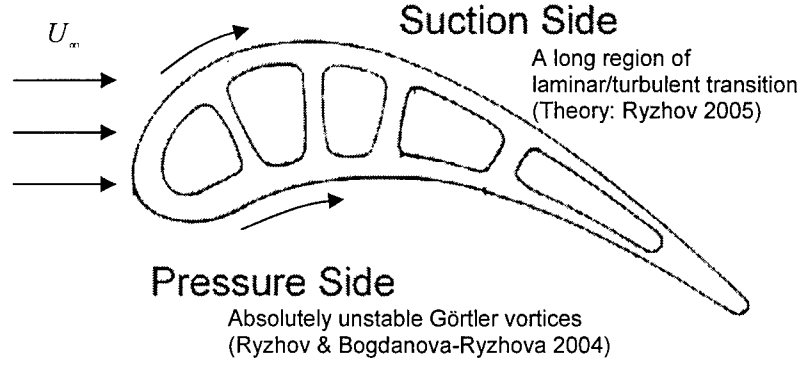


**Figure.**

## Part I: Görtler vortices

As it has been proposed, the formulation with the vibrating ribbon was chosen for simulating basic properties occurring in real turbomachinery environment as well as experimental setups.

### 1. Receptivity

Within the framework of an asymptotic approach based on the triple-deck theory, the initial system of Navier-Stokes equations reduces in the viscous near-wall sublayer to a much simpler set of Prandtl equations ( Stewartson 1974 )

$$\begin{aligned}
 \frac{\partial u}{\partial x} + \frac{\partial v}{\partial y} + \frac{\partial w}{\partial z} &= 0 \\
 \frac{\partial u}{\partial t} + u \frac{\partial u}{\partial x} + v \frac{\partial u}{\partial y} + w \frac{\partial u}{\partial z} &= -\frac{\partial p}{\partial x} + \frac{\partial^2 u}{\partial y^2} \\
 \frac{\partial w}{\partial t} + u \frac{\partial w}{\partial x} + v \frac{\partial w}{\partial y} + w \frac{\partial w}{\partial z} &= -\frac{\partial p}{\partial z} + \frac{\partial^2 w}{\partial y^2}
 \end{aligned} \tag{1a,b,c}$$

for an incompressible boundary layer, no matter what the Mach number of the oncoming flow. The pressure  $p = p(t, x, z)$  not known in advance from a solution of the Euler equations is to be determined simultaneously with the velocity field and the instantaneous displacement thickness  $-A(t, x, z)$ . Crossflow vortical disturbances obey

$$p = -\frac{1}{2\pi} \int_{-\infty}^{\infty} \int_{-\infty}^{\infty} \frac{\partial^2 A(t, \xi, \zeta) / \partial \xi^2}{\left[ (1 - M_\infty^2)^{-1} (x - \xi)^2 + (z - \zeta)^2 \right]^{\frac{1}{2}}} d\xi d\zeta - \varepsilon D \frac{\partial^2 A}{\partial z^2} \tag{2}$$

whereas unsteady Görtler vortices are controlled by ( Ryzhov & Bogdanova-Ryzhova 2003)

$$p = -\frac{1}{2\pi} \int_{-\infty}^{\infty} d\xi \int_{-\infty}^{\infty} \frac{\partial^2 A(t, \xi, \zeta) / \partial \xi^2}{\left[ (1 - M_\infty^2)^{-1} (x - \xi)^2 + (z - \zeta)^2 \right]^{\frac{1}{2}}} d\zeta + \varepsilon^3 HA \quad (3)$$

Here  $\varepsilon D$  and  $\varepsilon^3 H$  are similarity parameters, the wall curvature  $\kappa$  is included in  $H$ ,  $\varepsilon \rightarrow 0$  as the Reynolds number  $\mathbf{Re} \rightarrow \infty$ . The size of disturbances is fixed by the pressure variations which are  $O(\varepsilon^2)$  while the amplitude of a perturbing agency is as small as  $O(\varepsilon^5)$ . When dealing with an orderly roughness, we introduce the time-dependence by means of a factor  $\exp(i\omega_0 t)$  for  $t > 0$  and assume the periodic obstacle geometry to be specified as

$$y_w(x, z) = \sigma f(x) \cos(m_0 z), \quad t > 0 \quad (4)$$

In this approach  $y_w(x, z) = 0$  for  $t < 0$ . The main focus is on disturbances emitted during the initial pulse mode at  $t$  close to 0 when the generation of highly modulated wave packets rather than harmonic Tollmien-Schlichting wave trains takes place. This is the crucial point of the mathematical model since the most amplifying wave packets propagate with the group velocity as distinct from the phase velocity determining the direction in which the Tollmien - Schlichting waves sweep downstream of a perturbing source (Landau & Lifshitz 1959). The group and phase velocities are different in general; accordingly, the modulated wave packets and periodic wave trains can be driven in the opposite direction.

On the assumption that a parameter  $\sigma$  entering (4) tends to 0, a solution to the receptivity problem based on the linearized equations (1a-c) reads

$$p = \Re \left( p_c e^{im_0 z} \right) \quad (4a)$$

$$p_c = \frac{\omega_0 i}{4\pi^2} \int_{l-j\infty}^{l+j\infty} d\omega e^{i\omega t} \frac{\Phi(\Omega)}{(\omega^2 + \omega_0^2) [\Phi(\Omega) - Q(k, m_0)]} \mathcal{J}(x, k, m_0, M_\infty, S) \quad (4b)$$

with  $S$  standing for either of the two similarity parameters  $\varepsilon D$  or  $\varepsilon^3 H$  depending on whether the crossflow or Görtler vortices are under consideration. Here  $\Phi(\Omega)$  is a well-known function expressed through the first derivative  $dAi(\Omega)/dY$  and an improper integral

$$\begin{aligned} \mathcal{I}(\Omega) &= \int_{\Omega}^{\infty} Ai(Y) dY \text{ of the Airy function } Ai(Y) \text{ by means of} \\ \Phi(\Omega) &= \frac{dAi(\Omega)}{dY} \Gamma^{-1}(\Omega) \end{aligned} \quad (5)$$

The argument

$$\Omega = i^{-\frac{2}{3}} \omega K^{-\frac{2}{3}}, \quad K = k\tau_x + m_0\tau_z \quad (6a,b)$$

comprises the frequency  $\omega$ , both wavenumbers  $k$ ,  $m_0$  and the components  $\tau_x$ ,  $\tau_z$  of the wall shear stress. For wave system on a concave wall, we have  $\tau_z = 0$ ,  $k = 1$  and the generalized wavenumber simplifies to  $K = k$ . In this case the right-hand side of the dispersion relation

$$\Phi(\Omega) = Q(k, m_0) \quad (6)$$

takes the form

$$Q = i^{\frac{1}{3}} \frac{k^2 + m_0^2}{k^{\frac{5}{3}}} \left\{ \frac{k^2}{\left[ k^2 + (1 - M_\infty^2)^{-1} m_0^2 \right]^{\frac{1}{2}}} + \varepsilon^3 H \right\} \quad (7)$$

having a strong singularity  $k^{-\frac{5}{3}}$ . However the generalized wavenumber  $K$  determines an analogous singularity in the right-hand side

$$Q = i^{\frac{1}{3}} \frac{k^2 + m_0^2}{K^{\frac{5}{3}}} \left\{ \frac{k^2}{\left[ k^2 + (1 - M_\infty^2)^{-1} m_0^2 \right]^{\frac{1}{2}}} + \varepsilon D m_0^2 \right\} \quad (8)$$

of the dispersion relation (6) for crossflow vortices governed by the interactive law (2).

## 2. Residue series expansion

With real  $k$ , both positive and negative, the complex frequency plane has no branch points. Applying residue theorem to the Laplace integral in (4b) yields

$$\int_{l-i\infty}^{l+i\infty} d\omega e^{\omega t} \frac{\Phi(\Omega)}{(\omega^2 + \omega_0^2) [\Phi(\Omega) - Q(k, m_0)]} = \frac{\pi}{\omega_0} R_0 + 2\pi i R_1$$

$$R_0 = e^{i\omega_0 t} \frac{\Phi(\Omega_0)}{\Phi(\Omega_0) - Q(k, m_0)} - e^{-i\omega_0 t} \frac{\Phi(-\Omega_0)}{\Phi(-\Omega_0) - Q(k, m_0)} \quad (9a,b,c)$$

$$R_1 = \sum_{j=1}^{\infty} \frac{1}{\omega_j^2(k) + \omega_0^2} e^{\omega_j(k)t} \frac{\Phi(\Omega_j)}{\partial \Phi(\Omega_j) / \partial \omega}$$

where  $\Omega_0 = i^{\frac{1}{3}} \omega_0 K^{-\frac{2}{3}}$  and, in keeping with above abbreviations,  $\omega_j(k) = \omega_j(k, m_0) = i^{\frac{2}{3}} K^{\frac{2}{3}} \Omega_j(k, m_0)$ ,  $j = 1, 2, \dots$  are the dispersion relation roots. The first

term  $R_0$  in (9a) is periodic in time and has nothing to do with exponentially growing wave packets which are of primary concern for our purposes. As is known from the hydrodynamic stability theory, only the first root  $\omega_1$  in (9c) gives rise to unstable oscillations whereas all the other eigenmodes related to the roots  $\omega_j(k)$ ,  $j = 2, 3, \dots$ , damp out with time both upstream and downstream of the perturbing source. In an asymptotic representation for  $R_1$  we may confine ourselves to the leading-order approximation and write

$$R_1 \sim \frac{1}{\omega_1^2(k) + \omega_0^2} e^{\omega_1(k)t} \frac{\Phi(\Omega_1)}{\partial\Phi(\Omega_1)/\partial\omega}, \quad t \gg 1 \quad (10)$$

### 3. Reduction to single integrals

With (10) in hand, an inverse Fourier transform designated by  $\mathcal{J}(x, k; m_0, M_\infty, S)$  in (4b) reduces to

$$p_c = -\frac{i^{\frac{2}{3}}\omega_0}{2\pi} \int_{-\infty}^{\infty} dk e^{\omega_1(k)t + ikx} \bar{f}(k) \frac{K^{\frac{2}{3}} dAi(\Omega_1)/dY}{(\omega_1^2 + \omega_0^2) Ai(\Omega_1) [\Phi(\Omega_1) + \Omega_1]} \cdot \left\{ \frac{k^2}{\left[ k^2 + (1 - M_\infty^2)^{-1} m_0^2 \right]^{\frac{1}{2}}} + \varepsilon D m_0^2 \right\} \quad (11)$$

for crossflow vortical disturbances and

$$p_c = -\frac{i^{\frac{2}{3}}\omega_0}{2\pi} \int_{-\infty}^{\infty} dk e^{\omega_1(k)t + ikx} \bar{f}(k) \frac{k^{\frac{2}{3}} dAi(\Omega_1)/dY}{(\omega_1^2 + \omega_0^2) Ai(\Omega_1) [\Phi(\Omega_1) + \Omega_1]} \cdot \left\{ \frac{k^2}{\left[ k^2 + (1 - M_\infty^2)^{-1} m_0^2 \right]^{\frac{1}{2}}} + \varepsilon^3 H \right\} \quad (12)$$

for unsteady Görtler vortices. A study of the single integrals obtained presents a mathematical problem not nearly as complicated as the initial one given in (4b). Rigorous results based on (11) and (12) are set forth below.

### 4. Spectrum

In the Tollmien-Schlichting interval of frequencies and wavenumbers the first terms in curled brackets on the right-hand sides of (7) and (8) are dominant. The correction terms become comparable in magnitude to the leading-order terms within two spectral side bands. A high-frequency side band

$$\begin{aligned} \omega &= (\varepsilon D)^{-\frac{2}{7}} \omega_{cr} \approx 1.2 \omega_{cr} \\ k &= (\varepsilon D)^{-\frac{1}{7}} k_{cr} \approx 1.3 k_{cr} \end{aligned} \quad (13)$$

$$m_0 = (\varepsilon D)^{\frac{3}{7}} m_{cr,0} \approx 2.0 m_{cr,0}$$

specifies the range of unsteady crossflow vortices ( estimates here relate to a transitional boundary layer with Reynolds number  $\mathbf{Re} \sim 5 \cdot 10^5$  ). A low-frequency side-band

$$\begin{aligned} \omega &= (\varepsilon^6 H^2)^{\frac{1}{7}} \omega_G \approx 0.25 \omega_G \\ k &= (\varepsilon^9 H^3)^{\frac{1}{7}} k_G \approx 0.12 k_G \\ m_0 &= (\varepsilon^3 H)^{\frac{1}{7}} m_{G,0} \approx 2.0 m_{G,0} \approx 2.0 m_{cr,0} \end{aligned} \tag{14}$$

defines the range of unsteady Görtler vortices ( estimates are made with the same transitional Reynolds number ). Notice that the vortices of both types are equally packed in the spanwise direction and may be hardly discernable from each other if the three-dimensional (swept) and surface curvature effects simultaneously play an important role in creating centrifugal forces to balance out the normal-to-wall pressure gradient. Thus, the disturbance spectrum consists of the two side bands with the Tollmien-Schlichting interval of eigen frequencies in between.

## 5. Phase and group velocities

It is obvious from the large-time solution to the receptivity problem posed in (4) that the overall system of pulsations is determined by the behavior of the first root  $\omega_1$  of the dispersion relation (6) with the right-hand side prescribed either by (7) or by (8). The phase velocity

$$c = -\frac{\omega}{ik} \tag{15}$$

of the monochromatic Tollmien-Schlichting wave train differs from the group velocity

$$V_g = -\frac{d\Im(\omega_1)}{dk} \tag{16}$$

evaluated at the points where  $\Re(\omega_1)$  attains its global and local maxima. Since wave packets propagate at the group velocity, nothing can be said about the direction of their motion from (15) as it is sometimes done when predicting transition.

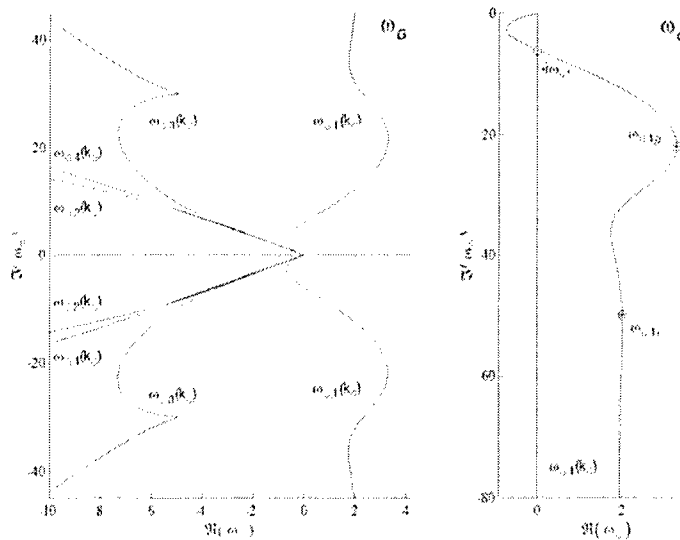


**Figure 1**

Figure 1 exhibits the complex frequency plane for Tollmien-Schlichting waves (using the Görtler variables with  $m_{G0} = 0$ ). The first dispersion curve  $\omega_{G1}$ , responsible for inducing unstable disturbances, consists of two branches positioned symmetrically about the real axis. Each branch involves the only lobe with

$$\frac{d\mathcal{I}(\omega_{G1})}{dk_G} < 0 \quad (17)$$

at every point. In this simplest case the directions of the phase and group velocities coincide with each other. The Blasius boundary layer offers an example marked by the conventional scenario of convective instability.

## 6. Mechanisms underlying streamwise absolute instability

The key issue is what happens to the boundary-layer stability properties under the action of centrifugal forces. The steepest descent method is best suited to solving this problem. The existence of saddle points of the phase function  $\varphi = \omega_1(k, m_0) + iV_s k$ ,  $V_s = x/t$  entering the exponent of the integrand in (11) and (12) is central to this method; their coordinates  $k_s = k_s(m_0, V_s)$  come from

$$\frac{d\omega_1(k)}{dk} + iV_s = 0 \quad (18)$$

A complete set of saddle points is needed to compute the pressure variations along an arbitrary ray  $x/t = \text{const}$ . It should be recognized that a saddle point  $k = k_s$  contributes to instability if the original integration path over the real axis can be continuously deformed into a steepest descent contour through this particular point. However we may put  $V_s = 0$  in (18) to settle the most significant issue of absolute instability in the streamwise direction.

The saddle point of the phase function specified by this condition becomes simultaneously a saddle point of the complex frequency. In numerous checks executed the original integration path in the Fourier transforms (11) and (12) was found to be deformable into the steepest descent contours through, respectively, the saddle points  $\omega_{cr1} = \omega_{cr1}(k_{cr}, m_{cr0})$  and  $\omega_{G1} = \omega_{G1}(k_G, m_{G0})$ . Thus we are left to conclude that absolute instability in the streamwise direction of the boundary layer is triggered by the vortical (crossflow or Görtler) disturbances in response to the initial pulse-like motion of the ribbon.

A close inspection of the shapes of the first dispersion curve in the crossflow and Görtler complex frequency planes reveals the mechanism of the streamwise absolute instability. Figure 2 shows that the first dispersion curve of crossflow oscillations falls apart into two branches located asymmetrically about the real axis. Each branch consists of two lobes. Both right-hand lobes having

$$\frac{d\Im(\omega_{cr})}{dk_{cr}} < 0 \quad (19)$$

are at the bottom of the conventional scenario of convective instability whereas the two left-hand lobes form a new crossflow eigenmode with

$$\frac{d\Im(\omega_{cr})}{dk_{cr}} > 0 \quad (20)$$

at any point.

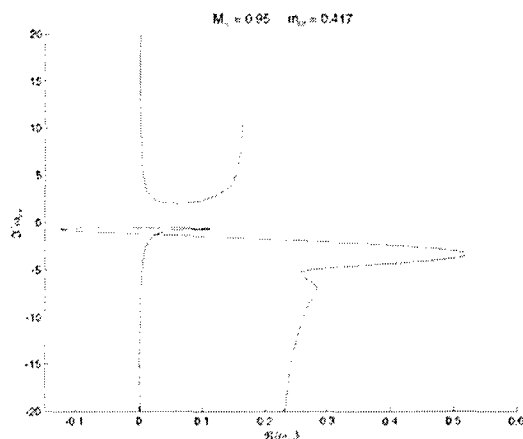
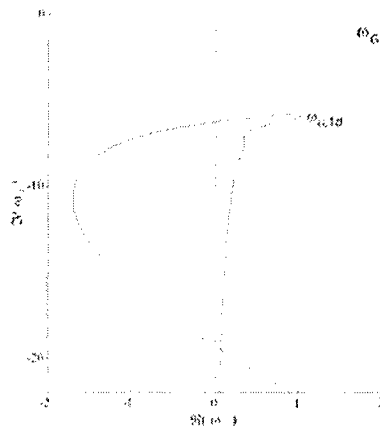


Figure 2

This vortical eigenmode controls oscillations in front of a site where they are given birth. What is more, the new eigenmode is endowed with a local peak  $d$  of  $\Re(\omega_{cr})$  at the tip of the loop that connects the right-hand and the left-hand lobes of the branch situated in the lower half-plane of the complex  $\omega_{cr}$ -plane. This local peak is responsible for emitting modulated wave-packets upstream, against the oncoming flow (Landau & Lifshitz 1959).



**Figure 3**

Figure 3 drawn with  $k_G > 0$  on an enlarged scale illustrates the formation of the loop in the lower branch of the first dispersion curve for Görtler vortical oscillations in the high subsonic Mach number regime. The upper branch corresponding to  $k_G < 0$  is a mirror image of the lower branch. As is obvious from this plot, the phase velocity  $c(k)$  defined by (15) is positive independent of the sign of  $k$ . Hence the harmonic wave trains propagate always downstream triggering convective instability of the boundary layer on a concave surface. On the contrary, modulated signals driven by the local peak  $d$  of  $\Re(\omega_G)$  and a similar peak on the upper branch advance upstream with the group velocity  $V_{gd} < 0$  according to (16). Thus it may be reasonably predicted from the curves in Figures 2 and 3 that exponentially amplifying oscillations develop not only in the immediate vicinity of a perturbing agency but move upstream of it in the form of wave packets consisting of long-scaled cycles (small  $k$ ). Upstream advancing signals underlie the mechanism of streamwise absolute instability provoked by the wave / vortex eigenmodes' interaction. Mathematically, the two-lobe structure of either of the two branches of the first dispersion curve is brought about by a singularity  $k^{-\frac{5}{3}}$  in the right-hand side of the dispersion relation (7) and an analogous singularity  $K^{-\frac{5}{3}}$  involved in (8).

## 7. Computed results

In line with the above theoretical predictions, the wave packets are seen in Figures below to form both downstream and upstream of the vibrating ribbon. No special thermal source was included in the computations where high frequency cycles were partially filtered out. The high subsonic Mach number regime brings out the significance of the streamwise absolute instability caused by the wave / vortex eigenmodes interactions at any value of  $M_\infty < 1$ .

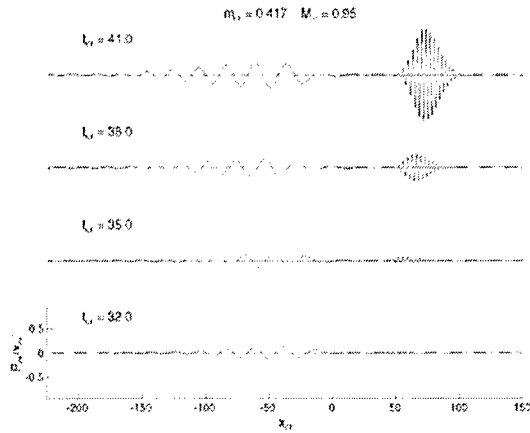


**Figure 4**

Figure 4 shows the wave system for the boundary layer with crossflow specified by  $m_{c,0} = 0.417$  and  $M_{\infty} = 0.95$ . The first dispersion curve in the complex crossflow frequency plane is depicted in Figure 2 for this case. Figure 5 gives the disturbance pattern for the boundary layer on a concave surface that corresponds to the first dispersion curve in the complex Görtler frequency plane of Figure 3. The downstream moving wave packets underlie the conventional route to convective instability. The upstream advancing wave packets are at the heart of streamwise absolute instability developing in front of a perturbing source. As predicted theoretically, streamwise

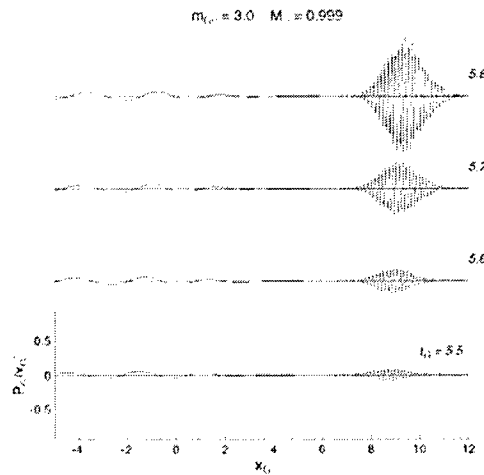


**Figure 5**

absolute instability is brought about by the new crossflow and Görtler-vortex eigenmodes endowed with positive values of  $d\mathcal{L}(\omega_1)/dk$ .

## References

1. Kachanov Y. S., Ryzhov O. S., Smith F. T. 1993 Formation of solitons in transitional boundary layers: theory and experiment. *J. Fluid Mech.*, 191, 273-297.
2. Landau L.D. & Lifshitz, E.M. 1959. *Fluid Mechanics*. Pergamon
3. Ryzhov O.S. & Bogdanova-Ryzhova E.V. 1997 Forced generation of solitary-like waves related to unstable boundary layers. *Adv. Appl. Mech.*, 34, 318-417.
4. Ryzhov O.S., Terent'ev E.D. 1998 Streamwise absolute instability of a three-dimensional boundary layer at high Reynolds numbers. *J. Fluid Mech.*, 373, 111-153.
5. Stewartson K. 1974. Multistructured boundary layers on flat plates and related bodies. *Adv. Appl. Mech.*, 14, 146-239.

## Part II: Laminar/turbulent transition on the convex side of a blade

### 1 Physical reasoning

External perturbing sources operating in the pulse mode generate strongly modulated wave packets in the Tollmien-Schlichting spectral range which cause transition to complete long before reaching the upper stability branch. The continuous filling-up of the wavenumber spectrum by the overlapping wings of neighbouring peaks gives rise to erratic short-scaled wiggles corrupting the primary long-scaled oscillation cycles. In this regard transition induced by the time-harmonic agency shows marked distinctions from the explosive transitioning to turbulence experienced by the wave packets. This simple preliminary consideration underlies the analysis below where the triple-deck formalism is exposed in more detail than in section 1. The extension is aimed at providing the clear understanding of the reasons why the powerful asymptotic approach that holds for laminar boundary layers, as it was initially designed, can be extended to transitional regimes.

### 2 Theory

Reasoning from the experimental findings of Gostelow, Hodson & Walker (1999) and Gostelow & Thomas (2005) that instabilities develop in the Tollmien-Schlichting spectral range, we begin with the triple-deck scheme set forth in Stewartson (1974). This approach leans upon asymptotic expansions in a small parameter

$$\varepsilon = \text{Re}^{-\frac{1}{8}}, \quad (2.1)$$

with  $Re$  being the characteristic Reynolds number. When considering experimental data,  $Re$  is as a rule evaluated with the distance  $L^*$  counted along a section from its nose. The empirical correlation by Mayle (1991) gives the transition length Reynolds number,  $Re_{lT}$ , for the blade suction side in terms of the momentum thickness Reynolds number at the end of transition,  $Re_{\theta T}$ , by

$$Re_{lT} = 75 Re_{\theta T}^{\frac{5}{4}}. \quad (2.2)$$

Thus, we have three Reynolds numbers:  $Re$  enters the asymptotic development whereas processing of experimental findings is based on  $Re_{lT}$  and  $Re_{\theta T}$ . Some comments are due at this point. Firstly, for a flat plate, the momentum thickness Reynolds number,  $Re_{\theta}$ , can be expressed through the displacement thickness Reynolds number,  $Re_{\delta}$ , as

$$Re_{\theta} = 0.3859 Re_{\delta}. \quad (2.3)$$

An analogous relationship holds for any airfoil section, with the numerical factor on the right-hand side depending on its shape. Secondly, within the framework of the high Reynolds number approach the transition length  $l_T^*$  is assumed to be much shorter than the characteristic distance  $L^*$ . Asymptotically, as  $\varepsilon$  tends to zero, (2.2) becomes

$$Re_{lT} = 22.81 Re_{\delta}^{\frac{5}{4}} \quad (2.4)$$

with the coefficient determined by using (2.3). Insofar as

$$Re_{\delta} = 1.7208 Re^{\frac{1}{2}}$$

for the Blasius boundary layer on a flat plate, we finally have an expression

$$Re_{lT} = 44.96 Re^{\frac{5}{8}} \quad (2.5)$$

defining the transition length  $l_T^*$  through the characteristic distance  $L^*$ . An analogous dependence is typical of an arbitrary blade or wing section. Asymptotically, (2.4) and (2.5) are tantamount to (2.2) and can be exploited as empirical correlations, however the results from wind-tunnel measurements collapse without appreciable scatter onto a straight line drawn by Mayle (1991) from (2.2). For this reason the momentum thickness Reynolds number seems to be preferable when processing experimental data.

Let  $\mu^*$  and  $T^*$  be the viscosity and temperature, respectively. With the subscript  $\infty$  labelling the conditions at the upper edge of the boundary layer, the Chapman-Rubesin linear law frequently used in theory reads

$$\frac{\mu^*}{\mu_\infty^*} = C \frac{T^*}{T_\infty^*}, \quad C = \text{const.}$$

The triple-deck time  $\frac{t^*}{\left(\frac{L^*}{U_\infty^*}\right)}$ , where  $U_\infty^*$  is the velocity of the oncoming stream, and spatial coordinates  $\frac{x^*}{L^*}$ ,  $\frac{y^*}{L^*}$  are scaled in terms of Reynolds number through the small parameter  $\varepsilon$  introduced in (2.1) and include the ratio  $\frac{T_w^*}{T_\infty^*}$  of the wall temperature  $T_w^*$  to the external temperature  $T_\infty^*$  as well as the Mach number  $M_\infty$  and the nondimensional skin friction  $\lambda = 0.3321$ , in the incompressible Blasius flow. For an arbitrary boundary layer, the skin friction  $\tau_w$  can be expressed through  $\lambda$  by means of  $\tau_w = \lambda C^{-\frac{1}{2}} \left(\frac{T_w^*}{T_\infty^*}\right)^{-1}$ . The above scaling defines a characteristic Strouhal number for free interaction. According to Stewartson (1974), Smith (1982), and Kluwick (1998), the independent variables in the viscous near-wall sublayer of the subsonic boundary layer are

$$\frac{t^*}{\left(\frac{L^*}{U_\infty^*}\right)} = \varepsilon^2 C^{\frac{1}{4}} \lambda^{-\frac{3}{2}} (M_\infty^2 - 1)^{-\frac{1}{4}} \left(\frac{T_w^*}{T_\infty^*}\right) t, \quad (2.6a)$$

$$\frac{x^*}{L^*} = \varepsilon^3 C^{\frac{3}{8}} \lambda^{-\frac{5}{4}} (M_\infty^2 - 1)^{-\frac{3}{8}} \left(\frac{T_w^*}{T_\infty^*}\right)^{\frac{3}{2}} x, \quad (2.6b)$$

$$\frac{y^*}{L^*} = \varepsilon^5 C^{\frac{5}{8}} \lambda^{-\frac{3}{4}} (M_\infty^2 - 1)^{-\frac{1}{8}} \left(\frac{T_w^*}{T_\infty^*}\right)^{\frac{3}{2}} y. \quad (2.6c)$$

Related to these normalized coordinates, the velocity field

$$\frac{u^*}{U_\infty^*} = \varepsilon C^{\frac{1}{8}} \lambda^{\frac{1}{4}} (M_\infty^2 - 1)^{-\frac{1}{8}} \left(\frac{T_w^*}{T_\infty^*}\right)^{\frac{1}{2}} u, \quad (2.7a)$$

$$\frac{v^*}{U_\infty^*} = \varepsilon^3 C^{\frac{3}{8}} \lambda^{\frac{3}{4}} (M_\infty^2 - 1)^{\frac{1}{8}} \left(\frac{T_w^*}{T_\infty^*}\right)^{\frac{1}{2}} v, \quad (2.7b)$$

and the pressure variations

$$\frac{p^* - p_\infty^*}{\rho_\infty^* U_\infty^{*2}} = \varepsilon^2 C^{\frac{1}{4}} \lambda^{\frac{1}{2}} (M_\infty^2 - 1)^{-\frac{1}{4}} p \quad (2.8)$$

obey the system of Prandtl equations

$$\frac{\partial u}{\partial x} + \frac{\partial v}{\partial y} = 0, \quad (2.9a)$$

$$\frac{\partial u}{\partial t} + u \frac{\partial u}{\partial x} + v \frac{\partial u}{\partial y} = -\frac{\partial p}{\partial x} + \frac{\partial^2 u}{\partial y^2} \quad (2.9b)$$

for an incompressible fluid, independent of the Mach number. The self-induced pressure  $p = p(t, x)$  comes from viscous/inviscid interaction rather than being given beforehand by a potential flow solution. In the absence of perturbing agencies, the pressure rises and drops are connected with the instantaneous displacement thickness  $-A(t, x)$  by the interaction law

$$p = \frac{1}{\pi} \int_{-\infty}^{\infty} \frac{\frac{\partial A(t, \xi)}{\partial \xi}}{x - \xi} d\xi. \quad (2.10)$$

The limit condition

$$u - y \rightarrow A(t, x) \quad \text{as } y \rightarrow \infty \quad (2.11)$$

at the upper reaches of the viscous near-wall sublayer and the no-slip condition

$$u = v = 0 \quad (2.12)$$

at the body surface make the mathematical formulation complete.

In order to extend the above consideration, we may drop the Chapman-Rubens viscosity law and introduce the independent variables through

$$\frac{t^*}{\left(\frac{L^*}{U_\infty^*}\right)} = \varepsilon^2 \tau_w^{\frac{3}{2}} (M_\infty^2 - 1)^{-\frac{1}{4}} \left(\frac{\mu_w^*}{\mu_\infty^*}\right)^{-\frac{1}{2}} t, \quad (2.13a)$$

$$\frac{x^*}{L^*} = \varepsilon^3 \tau_w^{-\frac{5}{4}} (M_\infty^2 - 1)^{-\frac{3}{8}} \left(\frac{T_w^*}{T_\infty^*}\right)^{\frac{1}{2}} \left(\frac{\mu_w^*}{\mu_\infty^*}\right)^{-\frac{1}{4}} x, \quad (2.13b)$$

$$\frac{y^*}{L^*} = \varepsilon^5 \tau_w^{-\frac{3}{4}} (M_\infty^2 - 1)^{-\frac{1}{8}} \left(\frac{T_w^*}{T_\infty^*}\right)^{\frac{1}{2}} \left(\frac{\mu_w^*}{\mu_\infty^*}\right)^{\frac{1}{4}} y \quad (2.13c)$$

instead of (2.6a-2.6c). The nondimensional velocity field and the pressure variations

$$\frac{u^*}{U_\infty^*} = \varepsilon \tau_w^{\frac{1}{4}} (M_\infty^2 - 1)^{-\frac{1}{8}} \left( \frac{T_w^*}{T_\infty^*} \right)^{\frac{1}{2}} \left( \frac{\mu_w^*}{\mu_\infty^*} \right)^{\frac{1}{4}} u, \quad (2.14a)$$

$$\frac{v^*}{U_\infty^*} = \varepsilon^3 \tau_w^{\frac{3}{4}} (M_\infty^2 - 1)^{\frac{1}{8}} \left( \frac{T_w^*}{T_\infty^*} \right)^{\frac{1}{2}} \left( \frac{\mu_w^*}{\mu_\infty^*} \right)^{\frac{3}{4}} v, \quad (2.14b)$$

$$\frac{p^* - p_\infty^*}{\rho_\infty^* U_\infty^{*2}} = \varepsilon^2 \tau_w^{\frac{1}{2}} (M_\infty^2 - 1)^{-\frac{1}{4}} \left( \frac{T_w^*}{T_\infty^*} \right)^{\frac{1}{2}} \left( \frac{\mu_w^*}{\mu_\infty^*} \right)^{\frac{1}{2}} p \quad (2.14c)$$

come in place of (2.7a, 2.7b) and (2.8), respectively. Here  $\tau_w$  and the ratio  $\frac{\mu_\infty^*}{\mu_w^*}$  depend on a particular boundary layer in question. The scaling in terms of  $\varepsilon$  as well as  $M_\infty$ -dependence remain intact, however the normalization that accounts for the temperature factor varies with the type of the boundary layer under consideration. Nonlinear stability of boundary layers for disturbances of various sizes was discussed by Smith (1979a).

The length  $l_i^*$  of the nonlinear interaction process governed by the system of Prandtl equations can be estimated as  $l_i^* \sim x^*$  with  $x^*$  defined in equations (2.6b) and (2.13b). Hence it follows that

$$l_i^* \sim \varepsilon^3 L^* = \text{Re}^{-\frac{3}{8}} L^*$$

in view of (2.1). The Reynolds number  $\text{Re}_{li}$  calculated with this characteristic length is expressed by virtue of

$$\text{Re}_{li} = \frac{l_i^*}{L^*} \text{Re} \sim \text{Re}^{\frac{5}{8}} \quad (2.15)$$

in terms of the Reynolds number. Thus, the transition length  $l_T^*$  in (2.4) exhibits the same scaling as the interaction length  $l_i^*$  in (2.15). In fact,  $l_T^*$  can be identified with  $l_i^*$  because evidently  $l_T^* \leq l_i^*$ . The result obtained goes far beyond the scope of the triple-deck theory which has been originally invented as applied to laminar boundary layers. The identity of the two lengths implies that the asymptotic approach extends to cover the regime of laminar/turbulent transition (except when the intermittency becomes close to 1).

Simple physical reasoning provides arguments substantiating this inference. The triple-deck scaling of time and spatial coordinates is typical of viscous/inviscid interaction. On the other hand, the same type of interaction is known to control the boundary-layer eigenmodes in the Tollmien-Schlichting spectral range centered about the lower branch of the neutral stability curve (Smith 1979b; Zhuk & Ryzhov 1980). Thus, the scaling introduced above specifies the period and wavelength of oscillation cycles within the Tollmien-Schlichting wave packets. The zone of transitional flow was recorded in numerous wind-tunnel tests to be filled with vortex spots (wave packets) that amplify exponentially fast and turn into turbulent spots coalescing with each other and thereby sharply increasing intermittency at later stages of transition. Between these spots the flow field remains laminar. So long as there is enough space between neighbouring spots they develop as if they were travelling in laminar surroundings. This is the reason why the transition and free interaction lengths have equal scaling in terms of the Reynolds number. Vigorous growth of the pulsation amplitudes within the spots does not change the scaling in (2.15) but can trigger erratic short wavelength wiggles to destroy the original well-organized vortex structures.

### 3 Numerical evidence

The last statement needs to be reinforced computationally. To this end, let us consider two mechanisms of the vortex-spot production.

**Wave-packet excitation by a convected vortex.** The first mechanism comes about by virtue of the potential vortex/surface roughness interaction. Strong similarities in the transition process between wake-induced turbulent patches on turbomachinery blades and artificially triggered turbulent spots in the flat plate boundary layer underlie this theoretical model. As mentioned, these similarities were exploited by Gostelow, Hodson & Walker (1999) and Gostelow & Thomas (2005) in their wind-tunnel tests to simulate the transition phenomena. Certainly, natural transition on turbomachinery blades is three-dimensional. However, in Gostelow & Thomas (2005) wakes were introduced into the flow by a tapered rod, of average radius 4.5 mm, cantilevered from a disk having axis 0.5 m upstream of the leading edge of the thin plate. The rod was mounted at a radius of 270 mm on the disk and was rotated at an angular velocity of 60 rpm, resulting in the introduction of two dissimilar wakes per second. Centerline phase-averaged velocity

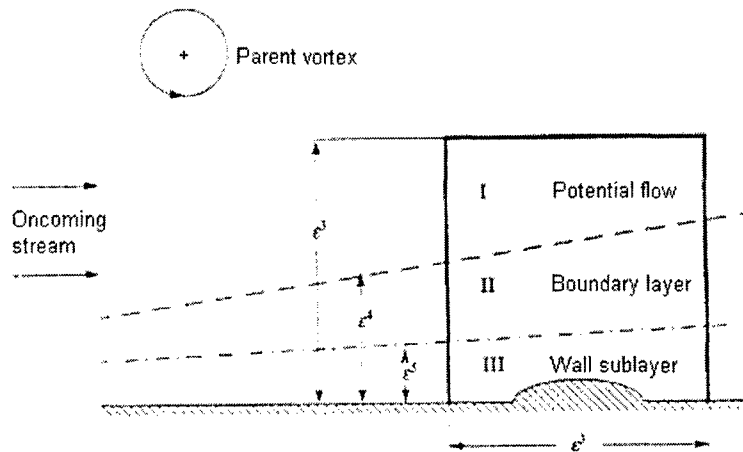


Figure 1: Schematic of vortex/hump interaction.

traces were obtained starting from the aforementioned similarities between the wake-induced turbulent patches and artificially excited turbulent spots. In fact, the convected-vortex model relates to conditions typical of the experimental set-ups rather than to the general case for which no wind-tunnel data are available.

Figure 1 gives an idea of the process and makes clear the triple-deck pattern of the velocity field with pertinent scalings involved. We point out briefly the most important features associated with the convected vortex. Asymptotically, as  $\epsilon \rightarrow 0$ , the flow in the near-wall sublayer obeys the system of Prandtl equations (2.9a, 2.9b). However an additional term is included in the expression (2.10) for the excess pressure to take into account the vortex-induced contribution. The limit condition (2.11) with the instantaneous displacement thickness entering the right-hand side also contains a correction  $p_v(t)$  for the vortex-induced pressure. This inhomogeneous limit condition at the upper edge of the near-wall sublayer should be supplemented with the inhomogeneous limit condition at the entry, as  $x \rightarrow -\infty$ , to the sublayer. The derivation of the inflow condition rests upon a detailed analysis of the vortex motion in a region upstream of the local roughness. Matching with the Stokes sublayer located close to the wall in this region shows that the instantaneous displacement thickness tends to zero as  $x \rightarrow -\infty$ , while the

vortex-induced velocity

$$U = -\frac{1}{2\pi} \int_{-\infty}^t \frac{y}{(t-\tau)^{\frac{3}{2}}} \exp\left[-\frac{y^2}{4(t-\tau)}\right] p_v(\tau) d\tau \quad (3.1)$$

provides the time-dependent contribution. In consequence,

$$u - y \rightarrow p_v(t) + U(t, y)$$

as  $x \rightarrow -\infty$ . The no-slip condition (2.12) applies at the body surface with a small hump or dent

$$y = y_w = ag(x) \quad (3.2)$$

centered around the origin.

Following Burggraf & Duck (1982) and Duck (1987) the boundary-value problem posed is recast by introducing the shear stress  $\tau(t, x, y)$  as a new desired function. Computing the Fourier spectral distribution

$$\bar{\tau}(t, k, y) = \frac{\partial \bar{u}(t, k, y)}{\partial y} = \frac{1}{2\pi} \int_{-\infty}^{\infty} \tau(t, x, y) e^{-ikx} dx$$

and then inverting it to the physical space

$$\tau(t, x, y) = \frac{\partial u(t, x, y)}{\partial y} = \frac{1}{2\pi} \int_{-\infty}^{\infty} \bar{\tau}(t, k, y) e^{ikx} dk$$

play a dominant role in an iteration procedure devised for an equation

$$\frac{\partial \tau}{\partial t} + u \frac{\partial \tau}{\partial x} + v \frac{\partial \tau}{\partial y} = \frac{\partial^2 \tau}{\partial y^2}$$

that arises upon differentiating (2.9b) with respect to  $y$ . Our main concern is with the onset of erratic wiggles in  $\tau_w = \tau(t, x, 0)$  accompanied with filling up the spectrum  $\bar{\tau}_w = \bar{\tau}(t, k, 0)$  with  $t$  increasing. A code with FFT algorithm has been tested in Ryzhov & Savenkov (1989) and Ryzhov & Timofeev (1995) when analyzing the short-scaled large-amplitude distortions appearing in a few central soliton-like cycles of the wave packets which can be identified with the vortex spots in laminar/turbulent transition. The geometry

$$g = \frac{1}{1+x^2}, \quad \bar{g} = \pi e^{-|k|} \quad (3.3)$$

assumed in the computation specifies a hump mounted on an otherwise flat plate, accordingly, the height of the obstacle in (3.2) being  $a = 1$ .

For better visualization of oscillation properties a quantity

$$\tau_w^d = \tau_w - 1 - \frac{\partial U(t, y)}{\partial y} \quad (3.4)$$

is meant by  $\tau_w^d$  in what follows. This quantity equals  $\tau_w^d = \tau_w - 1$  for the steady flow set in prior to the vortex motion that induces in line with (3.1) an additional component  $U(t, y)$  of velocity. The hump fixed by (3.3) introduces moderate disturbances in the velocity field of the oncoming steady stream without separation accompanied by a bubble with reversed flow (for separation to occur the height of the hump should be larger). The resulting boundary-value problem provides the simplest model of gas-turbine-engine environments where vortical disturbances interact with small imperfections of the turbine-blade surface (especially covered by the thermal barrier coating). Recent wind-tunnel tests by Pinson & Wang (2000) lend credence to the applicability of the transition-length correlation to rough surfaces.

Figures 2a, b, c show the origin and rapid development of a wave packet induced by a convected vortex interacting with the hump shaped by (3.2), (3.3). A value  $p_v^m = \max(|p_v|) = 3$  determines a fairly strong intensity of the vortex. At  $t = 0$ , the excess shear stress  $\tau_w^d$  is associated predominantly with the steady perturbations from the hump, the formation of unsteady oscillations downstream is barely discernible. The explosive character of the highly modulated wave packet propagation becomes clear at  $t = 1.5$  when a narrow soliton-like cycle appears in the central part of the signal. Figure 2c illustrates the onset at  $t = 2.5$  of short-scaled erratic wiggles that distort a portion of two central cycles of the wave packet with positive  $\tau_w^d$ . The soliton-like portions of the same cycles with negative  $\tau_w^d$  remain almost intact at this spiky stage typical of transition.

Figures 3a, b, c display the spectral content of disturbances shown in Figures 2a, b, c. The first of them presents the wavenumber spectrum of almost steady perturbations triggered by the hump, with the peak in  $|\tau_w^d|$  located approximately at  $k = k_s = 1.19$ . The second plot exhibits the spectrum featuring the wave packet at  $t = 1.5$ . The local maximum at  $k = k_s$  becomes much smaller compared to the local peak at about  $k = k_m = 2.75$  that corresponds to the wavenumber of the fastest growing linear eigenmode. The second local maximum at  $k \approx 2k_m = 5.5$  forks into two small mounds divided by a shallow local minimum in  $|\tau_w^d|$ . The third local smoothed-out

maximum arises at  $k \approx 3k_m = 8.25$ . One more local maximum is scarcely visible close to  $k \approx 4k_m = 11.0$ . Thus, the filling-up of the wavenumber spectrum basically follows a weakly nonlinear scenario in spite of the fact that the signal in Figure 2b is essentially nonlinear. To the contrary, the filling-up of the distant parts of the spectrum in Figure 3c is at the heart of the short-scaled wiggles corrupting two central cycles of the signal in Figure 2c. Here the first two peaks in  $|\tau_w^d|$  become almost equal whereas the other local maxima attain the magnitudes comparable to these peaks. The signal as a whole nears to transitioning to a turbulent spot. This process embracing all the vortex spots in the boundary layer eventually brings up the intermittency close to 1.

**Acoustic wave/surface roughness interaction.** The second mechanism of the vortex spot production comes about by virtue of sound scattering into Tollmien-Schlichting eigenmodes by small streamwise variations in surface geometry. This mechanism is even more important as applied to aircraft wings rather than turbomachinery blades. Time-harmonic oscillations were studied by Goldstein (1985) and Goldstein & Hultgren (1989). The closest resemblance to the wave-packet excitation by a convected vortex shows the propagation of a sound pulse impinging against a local obstacle located on an otherwise smooth surface (Ryzhov & Timofeev 1995). However there exists a difference between the two problems because a fluid in the potential flow domain cannot be regarded anymore to be incompressible even if velocities are small. The Mach number and temperature ratio dependencies should be incorporated into a set of similarity parameters in a manner specified in (2.6a-2.6c), (2.7a, 2.7b) and (2.8), or (2.13a-2.13c) and (2.14a-2.14c). The system of incompressible Prandtl equations (2.9a, 2.9b) still controls the flow field in the viscous near-wall sublayer where the excess pressure related to the instantaneous displacement thickness obeys (2.10) with an additional term accounting for sound scattering at subsonic velocities. What is more, the form  $f(t)$  of the sound pulse can be defined in such a way as to render it identical to a function  $p_v(t)$  that was used above to prescribe the vortex-induced pressure. This analogy enables the wave-packet excitation by a convected vortex to be experimentally simulated by means of acoustic generators.

Instead of applying this analogy we put in the computation

$$\begin{aligned} f &= 0 && \text{for } t < 0 \\ f &= 0.1\omega t \exp(1 - \omega t) && \text{for } t \geq 0 \end{aligned}$$

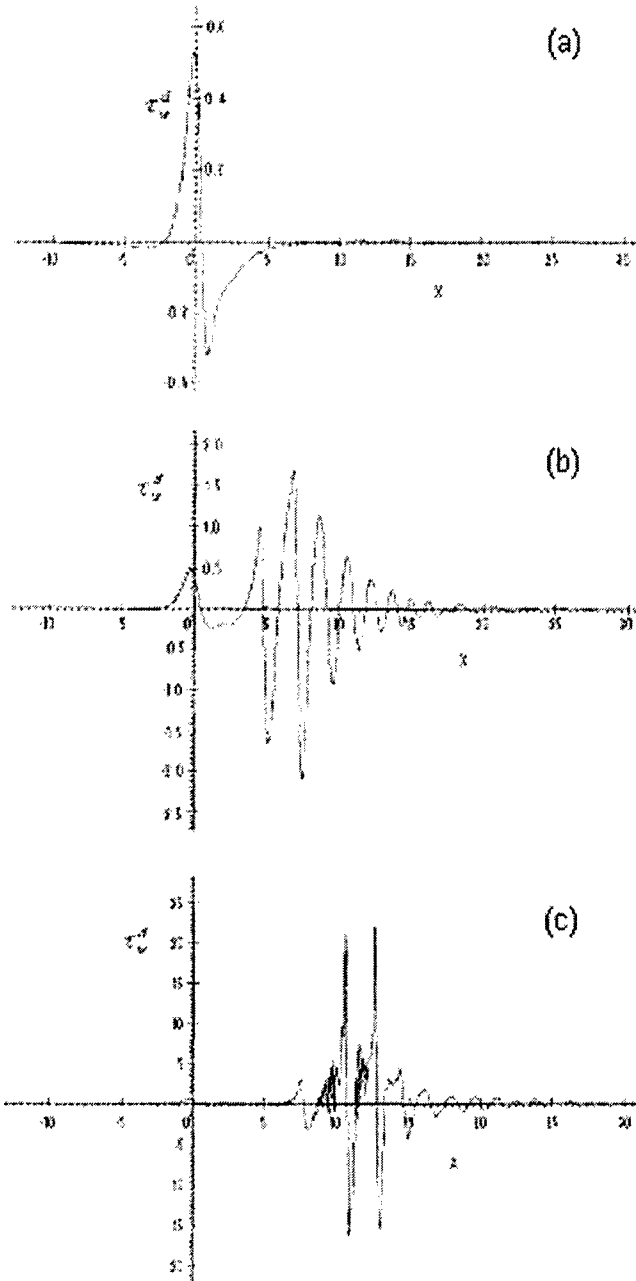


Figure 2: Wall-shear variations in the wave packet induced by a convected vortex. (a)  $t = 0$ ; (b)  $t = 1.5$ ; (c)  $t = 2.5$ .